Electronic Supplementary Material (ESI) for Nanoscale.

Supporting Information

Photoacid-Macroion Assemblies: How Photo-Excitation Switches the Size of Nano-Objects

Alexander Zika[a], Mohit Agarwal[a,b], Wiebke Zika[c], Dirk M. Guldi[c], Ralf Schweins[b], Franziska Gröhn[a*]

Abstract: Electrostatic self-assembly of photoacids with oppositely charged macroions yields supramolecular nano-objects in aqueous solutions, whose size is controlled through light irradiation. Nano-assemblies are formed due to electrostatic attractions and mutual hydrogen bonding of the photoacids. Irradiation with UV light leads to the deprotonation of the photoacid and, consequently, a change in particle size. Overall, the hydrodynamic radii of the well-defined photoacid-macroion nano-objects lie between 130 and 370 nm. For a set of photoacids, we determine the acidity constants in the ground and excited state, discuss the sizes of photoacid-macroion nano-objects (by dynamic and static light scattering), their composition, the particle shapes (by small-angle neutron scattering), and relate their charge characteristics to size, structure and shape. We investigate the association thermodynamics and relate nanoscale structures to thermodynamics and, in turn, thermodynamics to molecular features, particularly the ionization energy of the photoacid hydroxyl group proton. Structure-directing effects completely differ from those for previously investigated systems, with hydrogen bonding and entropic effects playing a major role herein. This combined approach allows developing a comprehensive understanding of assembly formation and photo-response, anchored in molecular parameters (pKa, ionization energy, substituent group location), charge characteristics, and the association enthalpy and entropy. This fundamental understanding again paves the way for tailoring application solutions with novel photoresponsive materials.

Table of Contents

Experimental Procedures

Chemicals and synthesis. The poly(amido amine) dendrimer of generation 4 (PAMAM, G4) was purchased from Dendritech (Midland, MI, USA). Photoacids 1-naphthol-3,6-disulfonate (>90%) and 2-naphthol-2,7-disulfonate (≥95%) were purchased from Sigma Aldrich (Munich, Germany), photoacid 1-napthol-3,8-disulfonate (≥95%) from abcr-GmbH (Karlsruhe, Germany), photoacid 2-naphthol-6,8-disulfonate from TCI Deutschland GmBH (Eschborn, Germany) and photoacid 2-naphthol-3,6,8-trisulfonate from Fujifilm wako (Neuss, Germany).

1-naphthol-4,8-disulfonate was synthesized as part of this study following a literature-known procedure.[81] For the synthesis, 1,8-naphthosulton was purchased from Sigma Aldrich (Munich, Germany). Deionized water was filtered with two 25 mm syringe filters, which possess a hydrophile membrane consisting of polytetrafluoroethylene with a pore size of 200 nm. 1,8-naphthosulton was dissolved in sulfuric acid and heated to 80°C under reflux for one hour. Thereafter, this mixture was added to ice and water. At room temperature, anhydrous sodium sulfate was added and the product was collected by filtration and dissolved in water again. By adding sodium chloride (25% w/v), the product was precipitated and again collected by filtration. The last step entails dissolving the pink solid in water at pH = 12 by adding NaOH. To complete the hydrolysis, the solution was stirred for 2h at room temperature. The product was in form of a pink solid after drying the solid in a vacuum.

Before the preparation of the sample, a stock solution of each chemical was prepared in deionized water and filtered through Millex-LG (Sigma-Aldrich, Munich, Germany) water set to pH of 7.0. The pH was determined with a HI 221 Microprocessor pH meter and adjusted by adding NaOH or HCl (1N, filtered with Millex-LG filter). For the photoacids, their stock solutions were stored in the dark. After the addition of the photoacid to the water, the dendrimer was added to the solution under stirring and light exclusion and the assemblies were characterized after 2 minutes of stirring. For every sample, the final concentration (1×10^{-4} mol/l) of the photoacid was kept constant. The concentration of the dendrimer varied according to the anticipated charge ratios. The samples were stable for at least a week before and after irradiation. Structures discussed represent equilibrium as can be concluded from different assembly pathways and multiple switching cycles leading to the same results.

For UV light irradiation, a UV lamp UVLM-28 EL from analytikjena with 8 W was used.

For the purpose of centrifugation, a centrifuge SIGMA 2-16K with a maximum speed of 15300 rpm was used. It was equipped with an angle rotor (no. 12148), which has a capacity of 24 × 1.5 mL and a maximum relative centrifugal force of 24 × 5 g. As it was impossible to spin everything down before irradiation, dialysis was performed for one week. For that, Float-a-lyzer dialysis tubes from Sigma-Aldrich with a molecular weight cutoff of 100 kDa were used, while Milli-Q water was adjusted to pH = 7.0.

Mid-IR spectroscopy measurements were carried out using a Shimadzu FT-IR Prestige 21 equipped with an ATR unit. Using transmittance mode, samples were measured in the solid state. The spectra were averaged over 20 runs and evaluated using the Origin Software.

Absorption spectra were recorded on a SHIMADZU UV Spectrophotometer (UV-1800) with a slit width of 1.0 nm and a range of 200 nm ≤ λ ≤ 800 nm. The spectra were recorded against air as a reference. For all measurements, 10 mm quartz cuvettes were used.

Dynamic light scattering (DLS) was carried out with the samples prepared as given above at ALV CGS 3 goniometer with an ALV 5000 correlator with 320 channels (ALV GmbH, Langen, German) using a red HeNe laser (λ = 632.8 nm, 20 mW). The samples were measured over a scattering angular range of 30° ≤ θ ≤ 150° in steps of 10° for a duration of 50 seconds. Through the Siegert relation, the intensity autocorrelation function $g^2(\tau)$ was transferred into the electric field autocorrelation function $g^1(\tau)$ (equation S1). The electric field autocorrelation function $g^1(\tau)$ was then transformed into the distribution of inverse relaxation times $A(\Gamma)$ by a regularized inverse

Laplace transformation (based on equation S2). Here, the The apparent diffusion coefficients D_{app} were calculated from the inverse relaxation time Γ by equation S3.

$$g^1(\tau) = B\sqrt{g^2(\tau) - 1} \quad \text{(S1)}$$

$$A(\Gamma) = \frac{1}{2\pi}\int_0^\infty g^1(\tau)e^{-\Gamma\tau}d\tau \quad \text{(S2)}$$

$$D_{app} = \frac{\Gamma}{q^2} \quad \text{(S3)}$$

with the scattering vector q. The diffusion coefficients D_0 were then obtained via extrapolation to zero scattering vector square. For diffusive processes, this extrapolation is needed as an angular dependency may results for a real (non-ideal) system due to the size distribution, intramolecular interactions and internal modes.[82-93] The hydrodynamic radii R_H resulted via the Stokes-Einstein relation (equation S4). The width of the size distribution is represented by the standard deviation σ resulting from the regularized inverse Laplace transformation.

$$R_H = \frac{k_B T}{6\pi\eta D_0} \quad \text{(S4)}$$

Due to the addition of salt by adjusting the pH-value (0.02M) the intermolecular interaction is screened and the counterion cloud is reduced, which can be seen in the monodisperse DLS measurements.[18, 94-96] To ensure the validity of the results, each charge ratio was prepared three times and measured with DLS and SLS. Consequently, the error bars represent the standard deviation derived from these three measurements.

Static light scattering (SLS) was measured with the same setup. In static light scattering, the average sample, solvent (water), and standard (toluene) scattering intensities were recorded in dependence on the scattering angle. Guinier Plots of ln (I) versus q^2 yielded intensities at scattering angle zero by extrapolation, and the radius of gyration R_G from the slope. The scattering intensity I_0 at zero scattering vector is proportional to the particle number concentration and the scattering contrast of one particle. The scattering of one particle - roughly approximated (assuming constant density) - is proportional to its volume given by the hydrodynamic particle volume:

$$V = \frac{4}{3}\pi R_H^3 \quad \text{(S5)}$$

and dividing I_0 by the relative scattering intensity of one particle (given by its volume) $I_{rel,\ one\ particle}$ thus yields an estimate of the particle number concentration.

ζ-Potential measurements of the same samples measured in DLS were carried out with a Zetasizer Nano ZS analyzer with a 4 mW HeNe laser (λ = 633 nm; Malvern Instruments Ltd., U.K.). The solutions were placed in folded capillary cells (DTS 1070). After applying an electric field across the sample solution, the electrophoretic mobility was measured by means of laser Doppler anemometry. By using the Smoluchowski approximation (equation S6), the ζ-potential was calculated from the electrophoretic mobility with ε_r as the dielectrical constant, ε_0 as the vacuum permittivity and η is the viscosity. The measurements were performed at 20 °C and repeated three times to gain an average value.

$$\mu_E = \frac{\varepsilon_r \varepsilon_0 \zeta}{\eta} \quad \text{(S6)}$$

Small-angle neutron scattering (SANS) measurements were performed at the D11 instrument at the Institut Laue-Langevin (ILL), Grenoble, France. The proposal number of the beamtime was: 9-11-2039 [DOI: 10.5291/ILL-DATA.9-11-2039].[97] SANS samples were prepared in D_2O with photoacid concentrations of 0.35 gL^{-1} (1mM) and generation 4 dendrimer concentrations of 0.2 $2gL^{-1}$ (0.016mM) and transferred into Hellma 404-QS quartz cells with 2 mm path length. The employed neutron beam was 15 mm in diameter. At a neutron wavelength λ = 6.0 Å (FWHM 9%), three different sample-detector distances (1.7 m, 8 m, and 38 m) were used with collimation distances of 4 m, 8 m, and 40.5 m, respectively. A total scattering vector range of 0.018 $nm^{-1} \leq q \leq 4.9\ nm^{-1}$ was investigated. Scattered neutrons were detected using a multitube ^3He gas detector consisting of three detector panels: a central one with 192 horizontally oriented tubes, and a left and a right-side panel of each 32 vertically oriented tubes. Each tube is 1 m long with a pixel size of 4 mm along the tube, with the inner tube diameter being 8 mm. The detector is therefore composed of 256 × 256 pixels. 2D Data were corrected for empty cell scattering, electronic background, detector uniformity via the measurement of 1 mm H_2O scattering, and transmissions, using the Mantid software package. Data were put on an absolute scale via the attenuated direct beam intensity, which was measured per instrument configuration. Azimuthally averaged scattering curves were then used to subtract the solvent scattering and incoherent background.

The normalized SANS intensity can be written as:

$$I(q) = \emptyset V_{NP} (\Delta\rho_{SLD})^2 P(q) S(q) \quad \text{(S7)}$$

Here, $\emptyset$ denotes the volume fraction, V_{NP} refers to the particle volume, $\Delta\rho_{SLD}$ signifies the difference in scattering length densities between solute and the solvent, and *P(q)* is the particle form factor corresponding to the particle shape. The structure factor *S(q)* represents the interparticle correlations, which are considered to be equal to 1, as the samples have been diluted and contain added low-molecular mass salt (see DLS) in such a manner that there are no interparticle correlations in the measured q-range (which furthermore is evident from the measured SANS data themselves). For example, for a sphere[100] with radius R, the form factor is**:**

$$P(q) = Scale \left[\frac{3(\Delta\rho)(\sin(qR) - qr\cos(qR))}{(qR)^3}\right]^2 + Background \quad \text{(S8)}$$

Where,

1. Scale corresponds to the volume fraction
2. R is the sphere radius (Å)
3. $\Delta\rho$ is the scattering contrast, i.e. the difference in their scattering length densities (Å^{-2}),
4. Background is the incoherent background (cm^{-1})

For a core-shell sphere form factor is**:** [100]

$$P(q) = \frac{Scale}{V}\left[\frac{3V_c}{V}(\rho_c - \rho_s)\frac{sin(qR_c) - qR_c cos(qR_c)}{(qR_c)^3} + (\rho_s - \rho_{solv})\frac{sin(qR_s) - qR_s cos(qR_s)}{(qR_s)^3}\right]^2 + Background \quad \text{(S9)}$$

Where:

1. Scale = Intensity scaling
2. V = Volume of the whole Particle
3. V_c = Volume of the core
4. R_s = radius of the particle (radius + thickness) (Å)
5. R_c = Radius of the core
6. ρ_c = Scattering length density of the core (Å^{-2})
7. ρ_s = Scattering length density of the shell (Å^{-2})
8. ρ_{solv} = Scattering length density of the solvent (Å^{-2}),
9. Background = incoherent background (cm^{-1})

Before data analysis, the SANS data was merged with static light scattering (SLS) data to extend the low-q region (SLS: 0.0068 nm^{-1} ≤ q ≤ 0.025 nm^{-1}). The instrumental resolution, i.e. the uncertainty of the measured q values, has been considered in the fitting procedure using the experimentally determined instrumental resolution contained in the fourth column of the 1D normalized data files. The polydispersity is also taken into account, using a lognormal distribution of the radius and/or the shell in case of core-shell spheres.

Specifically, the program SasView 4.2.2 was used to fit the scattering data using various model form factors, an open-source project hosted on GitHub originating from the National Institute of Standards and Technology (NIST) driven software project DANSE. It supplies a software for fitting small-angle scattering data and through the collaboration of expert users has become a very comprehensive software which comprises numerous form factor and structure factor models. Sasview is supported by most of the large scale facilities which is reflected by the composition of the core development team and the different funding schemes that have contributed to it. There are a number of different fit optimizers available in Sasview, we used the Levenberg-Marquardt algorithm which is the standard method for non-linear data fitting. According to the P(q) formulae above, the size parameters were fit including polydispersity during fitting. Also the sample scattering length densities were fit, because due to the existence of free photoacid in the solution the particle composition is not directly given by the sample composition.

Time-correlated single-photon counting was undertaken using an Edinburgh FS5 spectrofluorometer. A Picoquant Vis/UV laser at 266 nm was used as excitation light source. Fit and lifetime analyses were performed with the FLUORACLE software of the instrument or by using Origin software. Samples were contained in 10×10 mm quartz cuvettes and purged with argon for 15 min.

Femtosecond and nanosecond transient absorption studies were performed with the HELIOS (0 to 5500 ps) or EOS system (1 ns to 350 µs) from Ultrafast Systems. The laser source was a Clark MXR CPA2110 and CPA2101 Ti: sapphire amplifier with a pulsed 1 kHz output centered at 775 nm with 150 fs pulse width. The excitation pulses for 320 nm were generated via frequency doubling of a 640 nm output generated with a noncolinear optical parametric amplification (NOPA). The bandwidth of the excitation pulse is < 15 nm. For the femtosecond experiments, the white light was generated by focusing the 775 nm fundamental output into a 2 mm (vis: 420 – 760 nm) or 1 cm (NIR: 800 –1500 nm) Sapphire disk. In the case of nanosecond experiments, the white light (370 –1600 nm) was generated by a supercontinuum laser source with a 2 kHz repetition rate and a pulse width of approximately 1 ns. Samples were contained in 2 x 10 mm quartz cuvettes and purged with argon for 15 min. Global Analysis of transient absorption data was performed with the GloTarAn software[101] and includes a chirp correction.

Isothermal titration calorimetry (ITC) was performed on a VP-ITC microcalorimeter from MicroCal, Northampton, MA. As a control, dilution experiments of the individual components were performed. For the dye-dendrimer experiment, one initial injection of 10 µL to

saturate the titration cell wall was followed by 27 injections of 10 µL each. The time span between subsequent injections was 300 s. All experiments were conducted at 25°C. Data analysis was performed with the modified model described and implemented in the MicroCal ITC data analysis software for Origin 7.0. We employed the so-called "sequential binding" model. It considers the interaction at multiple binding sites, not differing between identical or non-identical binding sites. Therefore, it is general and can be applied to any possible scenario with more than one ligand. Here, it is important to note that the name may be misleading, as the ligand binding is not sequential and the name derives from the math behind the binding model:

$$[X] + [M] \rightleftharpoons [(1-\mathrm{X})(1-\mathrm{M})]_{bound} \tag{S11}$$

$$K_1 = \frac{[MX]}{[M][X]} \qquad K_2 = \frac{[MX_2]}{[MX][X]} \qquad K_3 = \frac{[MX_3]}{[MX_2][X]} \tag{S12}$$

The fourth parameter, ΔG (free energy change), is calculated from the equilibrium constant K. Thus, the ΔS (entropy change) can then be calculated with the help of ΔH (enthalpy change).

$$\Delta G = -RT \ln K = \Delta H - T\Delta S \tag{S13}$$

DFT calculations were performed using the Spartan'14 software (Wave function Inc., Irvine, CA, USA, 2014) was used. Using a 6-31G* basis set in a vacuum, molecular properties and electrostatic potential surfaces were generated with the density functional B3LYP level of theory. All molecules were optimized for the equilibrium geometry with the dipole moment, the ionization energy and maxima and minima in the electrostatic potential surface determined.

Atomic force microscopy (AFM) was performed using NanoWizard 4 from a JPK instrument (Berlin, Germany) operated in tapping mode with a fixed-spring cantilever holder and a USC-F0.3-k0.3-10 ultrashort cantilever with a force constant of 0.3 Nm^{-1}. AFM samples were prepared by drop-casting the solution on a freshly cleaved mica substrate. Dendrimer–photoacid samples before and after irradiation were blow-dried after 10 min. The images were analyzed using Gwyddion 2.47.

Results and Discussion

Photoacid Characterization: Acidity Constants in the Photo-Excited State

As photoacids have different pK_as in their excited state compared to the ground state, sound knowledge of the strength of the different photoacids is paramount. For this reason, we determined the different pK_as of all photoacids. One way to determine the difference in the pK_as of the photoacids upon excitation is using the method of the so-called Förster cycle,[102,103] which is based on the ground state thermodynamics and electronic transition energies. It considers the difference in molar enthalpy change and uses the approximation, that the standard entropy change is zero. The relation is given in equation 15.

$$\Delta pKa = pKa - pKa^* = 0.00209 cm^{-1}(A_{UV/vis} - E_{Fluoreszenz}) \tag{S14}$$

Here, steady-state emission measurements of the protonated and deprotonated photoacids were carried out (Figure S1).

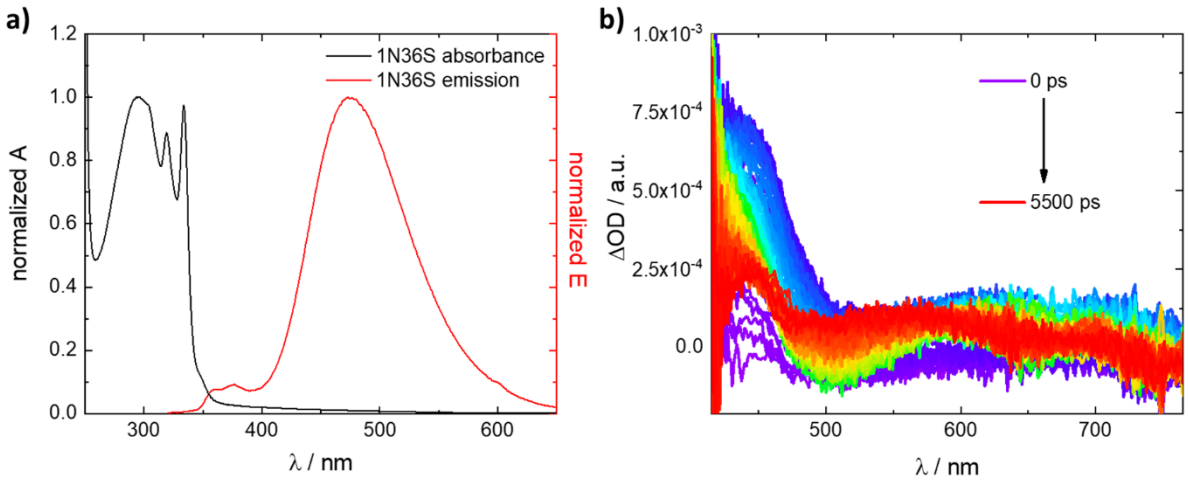

Figure S1: Analysis of the photoacidity of 1N36S: a) Steady-state absorption and fluorescence measurements; b) Transient absorption spectroscopic measurements.

The Förster cycle is an excellent starting point for a more accurate determination of the pKa* value of the photoacids, which directly measures the excited-state proton dissociation and recombination rates. Measurements were done using time-correlated single photon counting (TCSPC) and transient absorption spectroscopy (TAS). From TAS, at least three distinct states were found, decaying in a sequential manner. They correspond to the excited state ROH*, the dissociated excited state RO^-*, and the dissociated ground state RO^-. To determine pK_a*, only the first state is of interest. However, its decay includes fluorescence and dissociation. Therefore, TCSPC was measured to identify $k_{fluorescence}$. To exclusively determine the fluorescence lifetime of ROH* and not RO^-*, we carried out TCSPC measurements in DMSO to suppress any proton exchange. Then, the results from TAS and TCSPC measurements were put together to yield pK_a* using the following equations:

$$pKa^* = -\log\left(k_{dissociation} - k_{fluorescence}\right) \tag{S15}$$

with

$$k_{dissociation} = k_{TAS,state\,1} - k_{fluorescence} \tag{S16}$$

Table 1 displays the results of both methods. When comparing both approaches to determine the strength of the photoacidity, it is obvious that both are rather similar. The photoacids with the hydroxyl group placed at the carbon-1-position, in the following named 1-OH isomers (that is 1N36S, 1N38S, 1N48S, compare Scheme 1), in general, are the stronger photoacids, except for 2N368S due to the third sulfonate group. This trend has already been reported.[104-106]

Table S1: Strength of the different photoacids before irradiation (pK_a) and while irradiation (pK_a*) determined from the Förster cycle and the direct measurements.

	1N36S	1N38S	1N48S	2N36S	2N68S	2N368S
pK_a	8.6	8.78	8.74	8.99	8.94	8.89
pK_a*	-2.26	-0.64	-0.54	0.43	0.21	-0.7
pK_a-pK_a*	10.86	9.42	9.28	8.56	8.78	9.59
Förster cycle	10.84	8.94	8.47	8.43	8.22	9.31

Dynamic Light Scattering

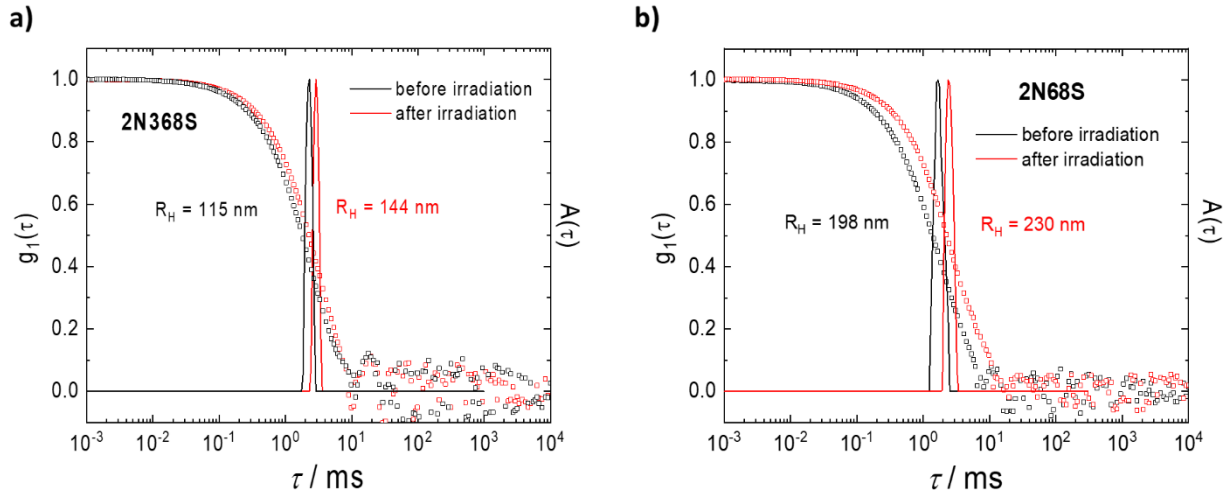

Figure S2: DLS of photoacid-macroion nano-objects before and after photo-irradiation: Electric field autocorrelation function $g_1(\tau)$ and distribution of relaxation times $A(\tau)$ at a scattering angle of $\theta = 90°$ for assemblies with a) 2N368S and b) 2N68S at $I = 4.0$, and corresponding hydrodynamic radii R_H resulting from the angular dependent DLS (c(photoacid) = $1 \cdot 10^{-4}$ mol/l).

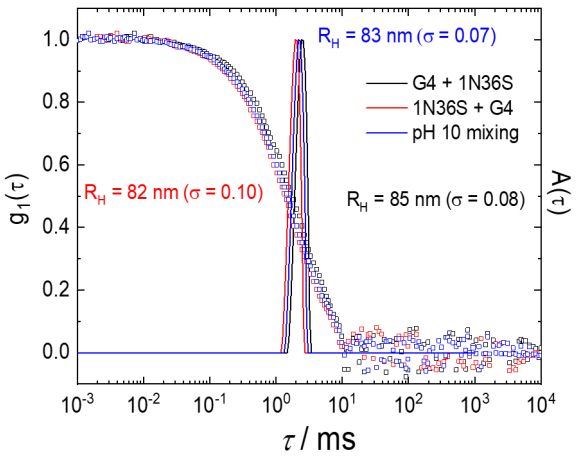

Figure S3: Influence of preparation procedure: DLS of photoacid-macroion nano-objects synthesized by various methods before photo-irradiation: Electric field autocorrelation function $g_1(\tau)$ and distribution of relaxation times $A(\tau)$ at a scattering angle of $\theta = 90°$ for assemblies with 1N36S ($I = 4.0$) , and corresponding hydrodynamic radii R_H resulting from the angular dependent DLS. Black: as mentioned in the experimental section, first G4 dendrimer, followed by the photoacid. Red: Mixing order is switched around by adding the photoacid first in aqueous solution followed by the addition of G4 dendrimer. Blue: Mixing the building blocks at pH = 10.0, and changing the pH afterwards to pH = 7.0.

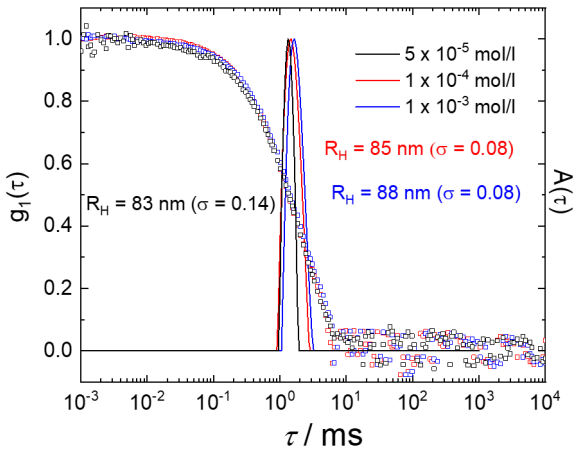

Figure S4: Influence of the concentration: DLS of photoacid-macroion nano-objects at various concentrations before photo-irradiation: Electric field autocorrelation function $g_1(\tau)$ and distribution of relaxation times $A(\tau)$ at a scattering angle of $\theta = 90°$ for assemblies with 1N36S, and corresponding hydrodynamic radii R_H resulting from the angular dependent DLS.

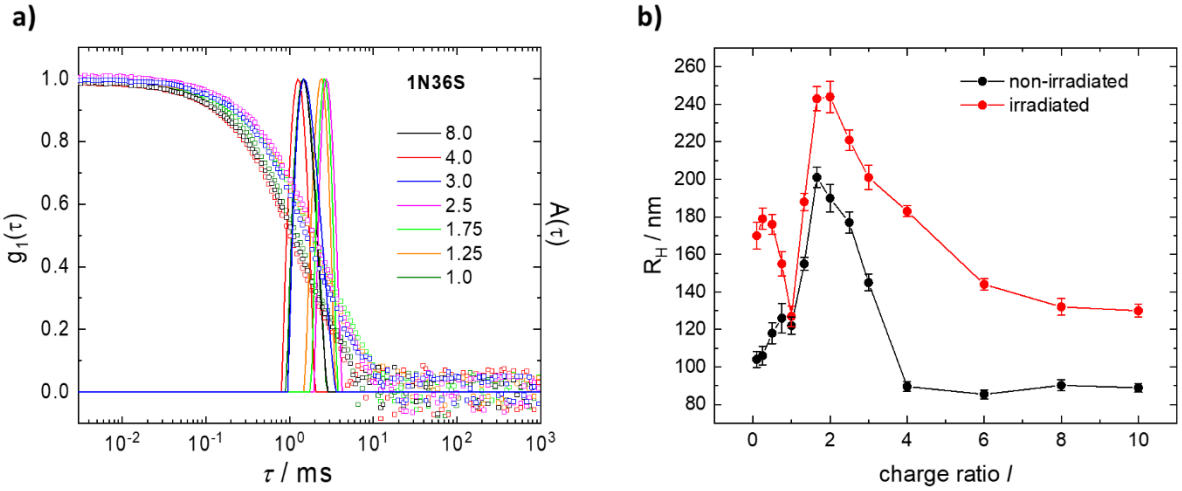

Figure S5: Influence of the charge ratio: a) DLS of photoacid-macroion nano-objects for the assemblies with 1N36S at different charge ratios before photo-irradiation: Electric field autocorrelation function $g_1(\tau)$ and distribution of relaxation times $A(\tau)$ at a scattering angle of $\theta = 90°$. (Extracted radii for further use result from the angular dependent extrapolation); b) hydrodynamic radii R_H of the photoacid-macroion nano-objects determined by DLS (c(photoacid) = $1 \cdot 10^{-4}$ mol/l) for 1N36S. The error bars of the DLS measurements were determined by averaging the R_H after measuring the sample three times.

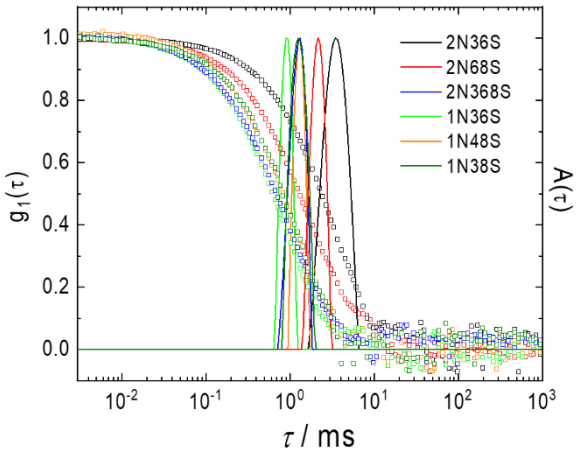

Figure S6: Influence of the photoacid: DLS of photoacid-macroion nano-objects of the different photoacids before photo-irradiation with a charge ratio of *I* = 4.0: Electric field autocorrelation function $g_1(\tau)$ and distribution of relaxation times $A(\tau)$ at a scattering angle of $\theta = 90°$.

Static Light Scattering Intensity

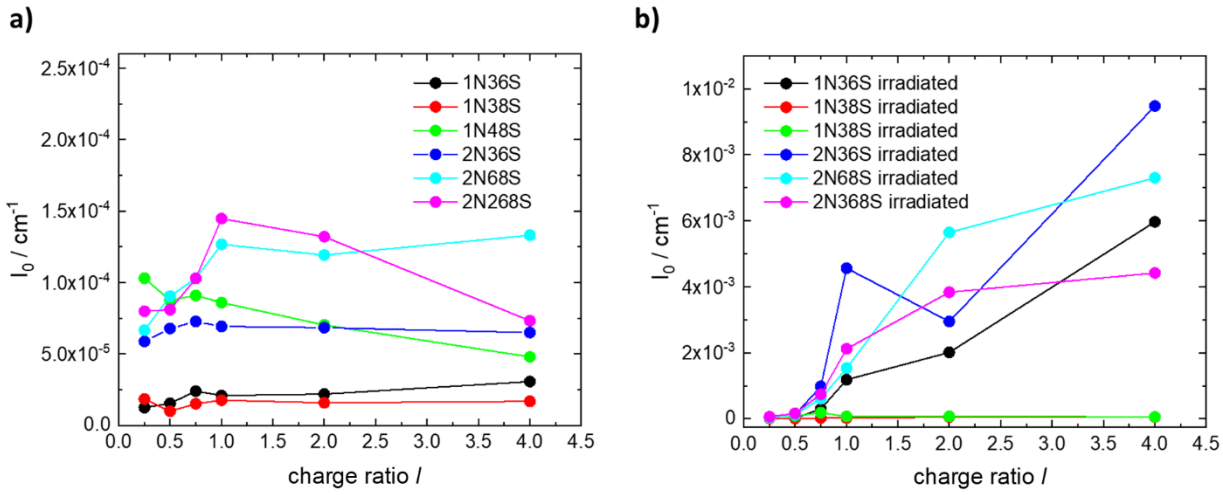

Figure S7: Light scattering intensity analysis of the photoacid-macroion nano-objects: a) before and b) after irradiation. The scattering intensity I_0 was determined by extrapolating to zero q, according to the Guinier approximation in a linear Guinier regime.

Composition Analysis

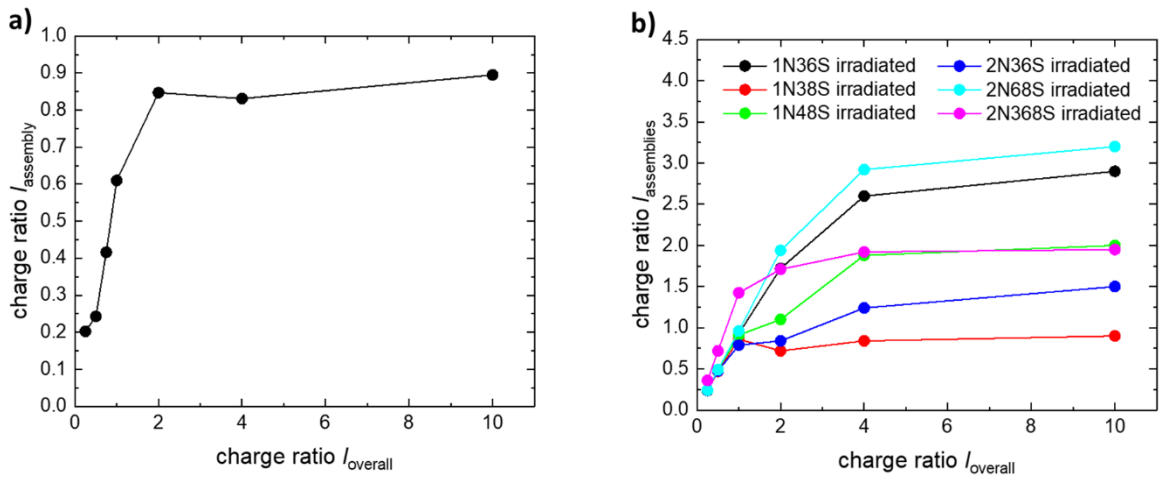

Figure S8: Composition of the photoacid-dendrimer assemblies: charge ratio of the assemblies $I_{assemblies}$ as a function of the prepared total charge ratio $I_{overall}$: a) before irradiation determined by dialysis (with 1N36S); b) after irradiation determined by centrifugation.

Static Light Scattering: Guinier Plots

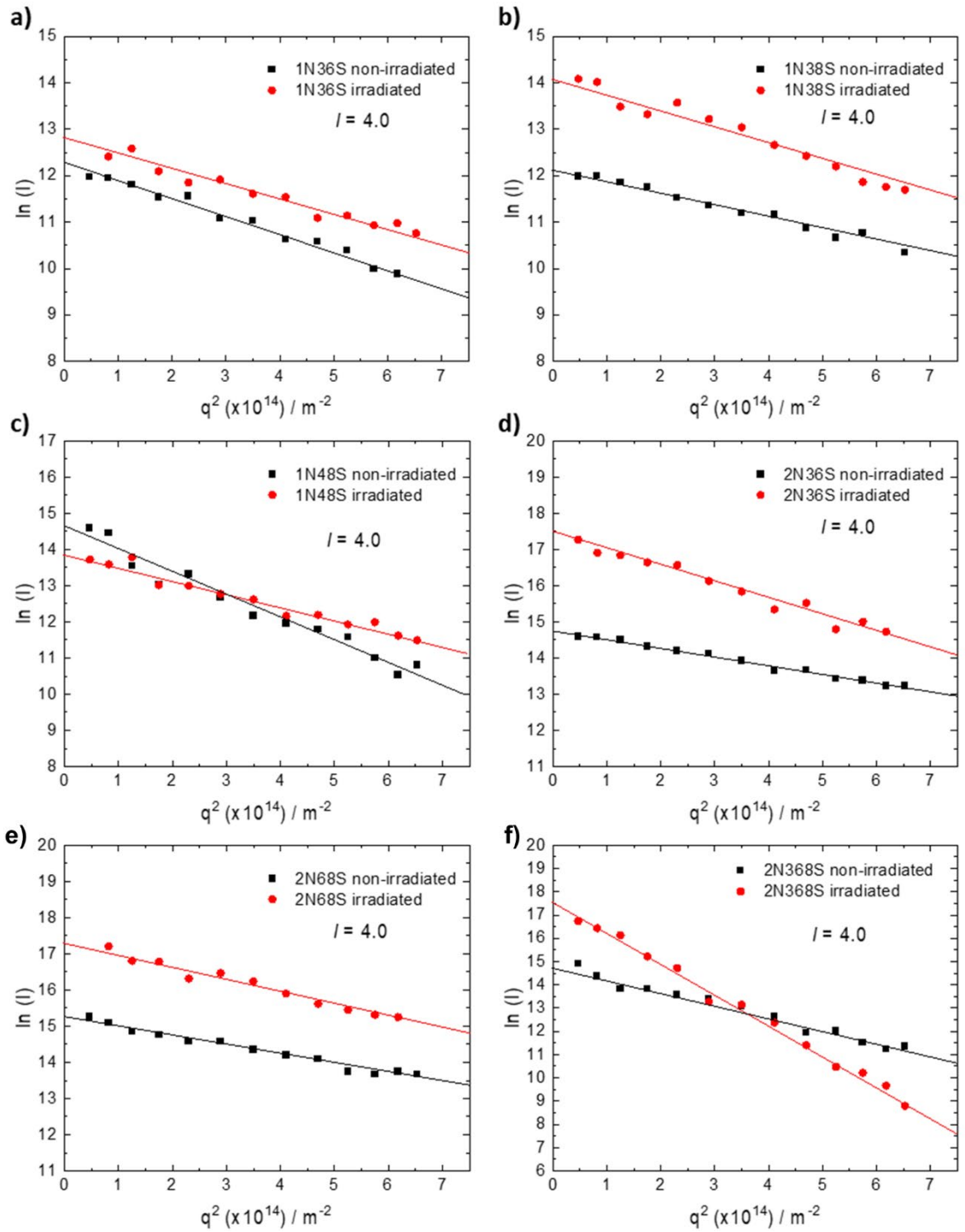

Figure S9: Static light scattering data for the assemblies with the different photoacids before and after photo-irradiation: a) 1N36S b) 1N38S c) 1N48S d) 2N36S e) 2N68S f) 2N368S.

Small-Angle Neutron Scattering

Table S2: SANS results of the photoacid-dendrimer assemblies with the different structures according to structural model fits.

Sample	Shape	Total Radius [a]	Shell-Thickness[b]	PDI[c]	χ^2
1N36S-G4, non-irradiated	Sphere	(2.5 ± 0.1) nm		0.04	1.20
	Core-shell sphere	(89.7 ± 0.44) nm	(43.6 ± 0.3) nm	0.21	
1N36S-G4, irradiated	Sphere	(180 ± 0.4) nm		0.001	2.85
2N36S-G4, non-irradiated	Sphere	(2.3 ± 0.03) nm		0.04	1.9
	Core-shell sphere	(98.2 ± 0.3) nm	(2.0 ± 0.4) nm	0.002	
2N36S-G4, irradiated	Sphere	(2.3 ± 0.15) nm		0.04	2.53
	Core-shell sphere	(127 ± 0.5) nm	(15.0 ± 0.6) nm	0.17	

[a] Total radius with the error bar, [b] Shell thickness with error bar, [c] Polydispersity index (relative width of the size distribution) and χ^2 (measure of the goodness of the fit). The error bars for radius and shell thickness result from the experimental error of the intensity (sum up of multiple runs) and the error propagation in the fitting of the structural model form factor to the data with experimental error. Given are the results for the best structural model fits (particle shapes) with the lowest χ^2. All other models showed much higher χ^2 and thus were not selected. SANS results given here are consistent with light scattering and LS-SANS Guinier analysis.

AFM Analysis

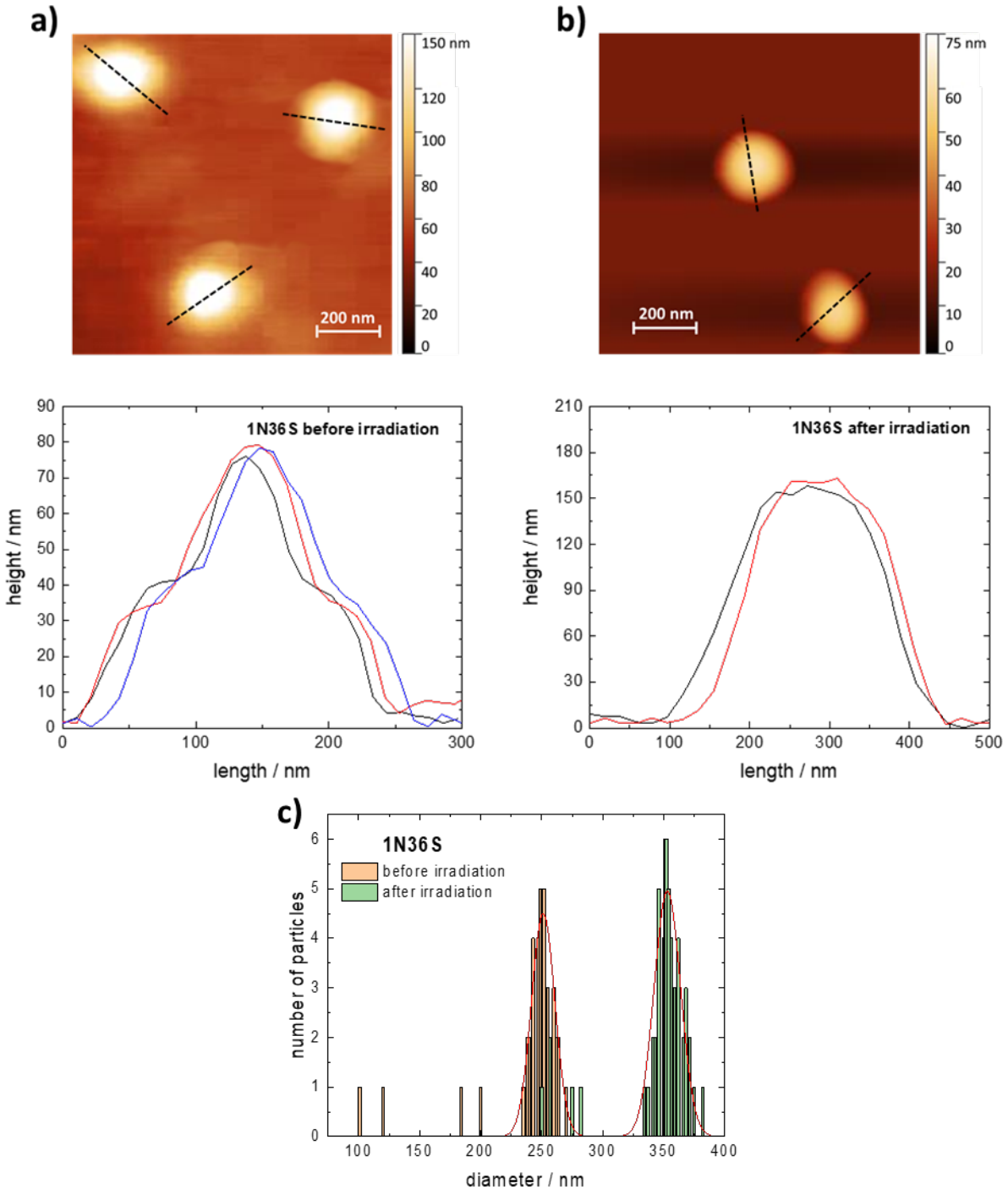

Figure S10: AFM of photoacid-dendrimer assemblies with 1N36S: top: height images, bottom: height profiles a) before photo-irradiation (core-shell structures) and b) after photo-irradiation (spheres). Before irradiation, the height profile shows two distinctive heights. The plateau around 40 nm corresponds to the shell, while the height of 80 nm crresponds to the core structure. After irradiation, only one height plateau can be observed suggesting a homogenous sphere. c) Statistic analysis of the photoacid-dendrimer assemblies before and after irradiation. Before irradiation, the particle size 240 nm ≤ d ≤ 270 nm with a mean value of d = 252 nm. Some smaller assemblies can be found which arise due to drying. After irradiation, an increase in size is observed to well-defined particles with a size 330 nm ≤ d ≤ 380 nm with a mean value of 350 nm. Some smaller assemblies can also be observed here, which correspond to non-irradiated assemblies. Overall, the particles are well defined with a standard deviation of 11 nm and 13 nm for the irradiated and non-irradiated case, respectively.

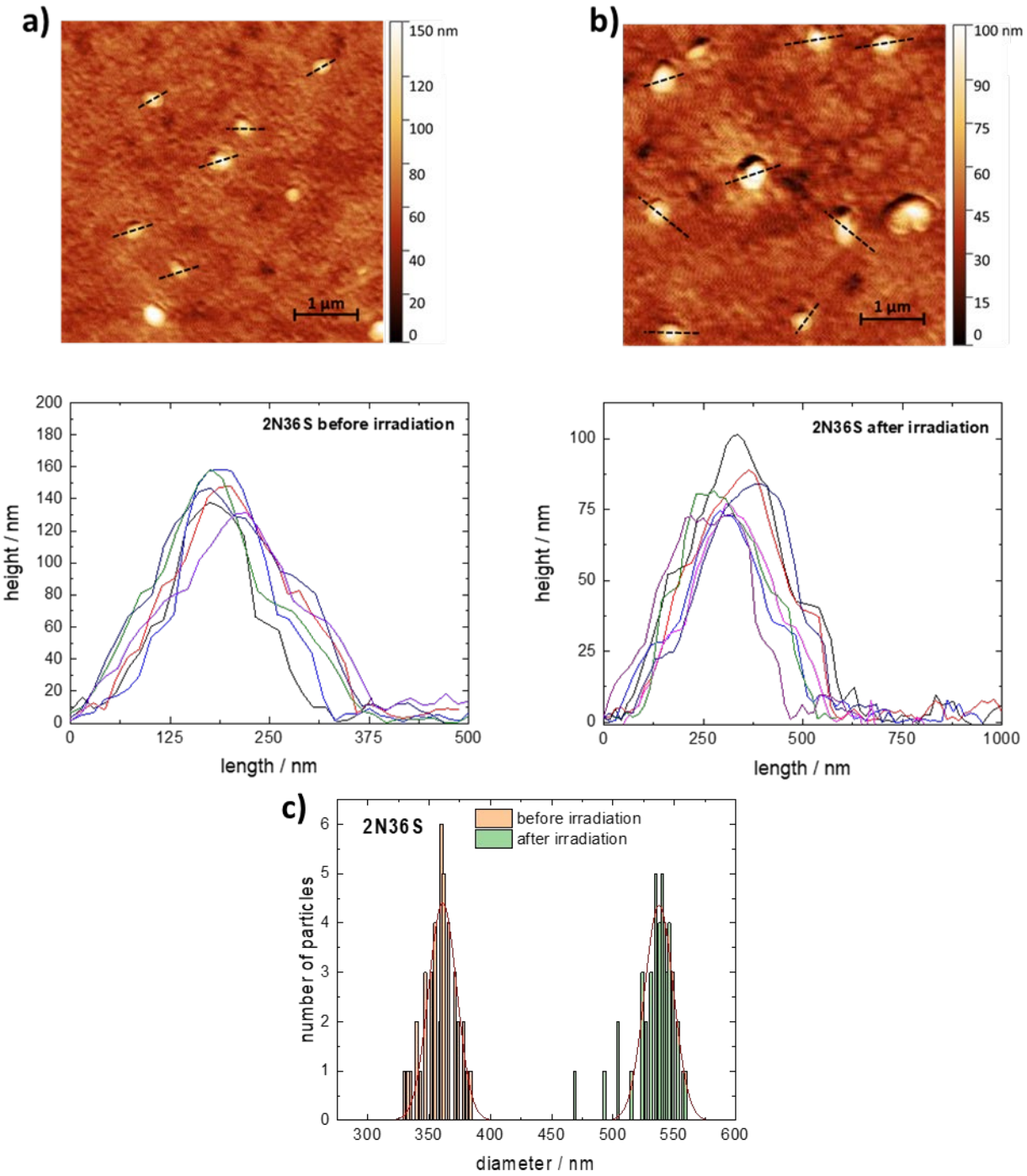

Figure S11: AFM of photoacid-dendrimer assemblies with 2N36S: top: height images, bottom: height profiles a) before photo-irradiation (core-shell structures) and b) after photo-irradiation (core-shell spheres). Before irradiation, the height profile shows two distinctive heights. The plateau around 60 nm corresponds to the shell, while the height of 160 nm corresponds to the core structure. After irradiation, the same behavior can be observed with a plateau at around 35 nm and 85 nm. c) Statistic analysis of the photoacid-dendrimer assemblies before and after irradiation. Before irradiation, the particle size 330 nm ≤ d ≤ 370 nm with a mean value of 360 nm. After irradiation, an increase in size is observed of well-defined particles with 500 nm ≤ d ≤ 560 nm with a mean value of 535 nm. Some smaller assemblies can also be observed here, which arise due to drying. Overall, the particles are well defined with a standard deviation of 17 nm and 24 nm, for the irradiated and non-irradiated case, respectively.

ζ-Potential Measurements

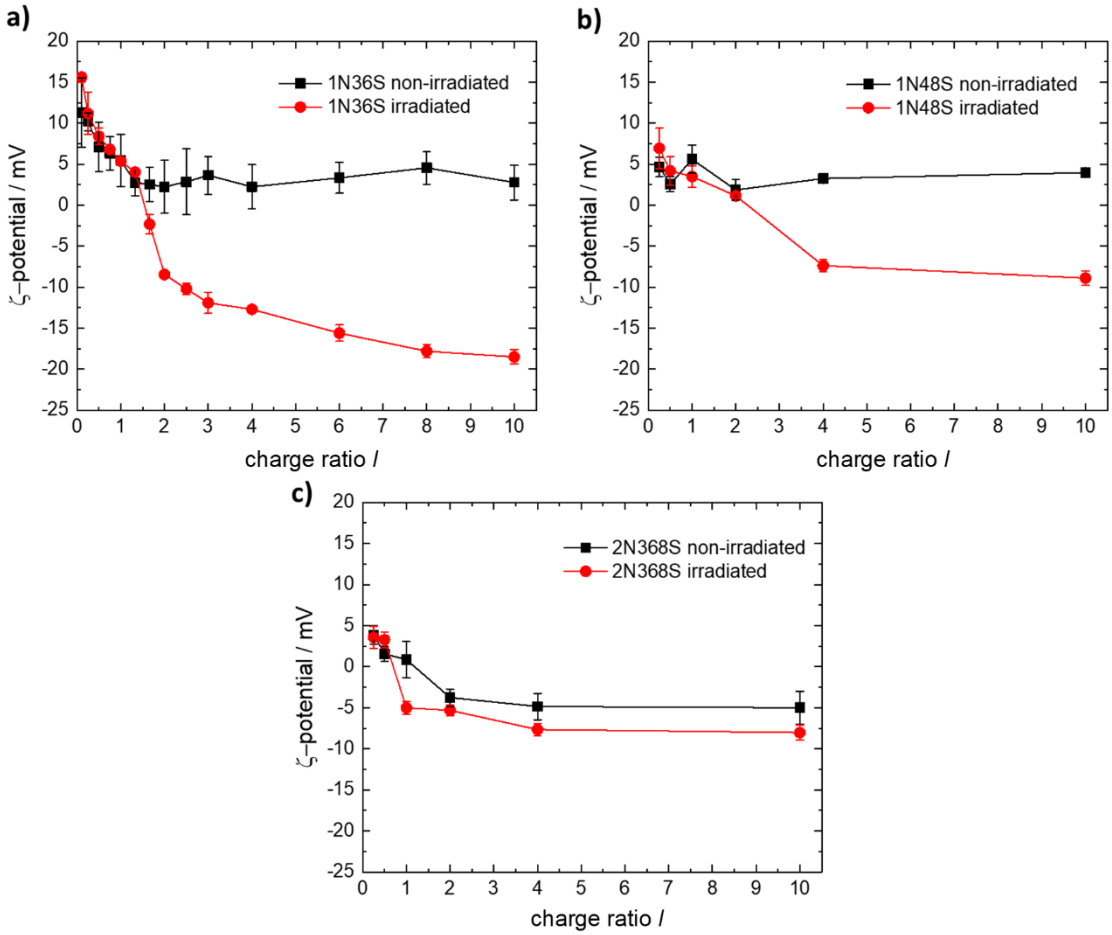

Figure S12: ζ-potential of nano-objects with a) 1N36S, b) 1N48S and c) 2N368S as a function of the charge ratio *I*.

Overview on Structural Parameters

Table S3: Overall summary of the important properties regarding the structural change after irradiation for the different photoacids (pos. = positive; neg. = negative).

	Structure	V_{AFM}/V_{DLS}	ζ-potential	Surface charge density	Charge density
1N36S	Core-shell -> sphere	0.31 -> 0.20	Pos. -> neg. (absolute value higher)	Pos. -> neg. (absolute value higher)	Pos. -> neg. (absolute value higher)
1N38S	Core-shell -> sphere	0.055 -> 0.046	Pos. -> closer to 0	Pos. -> depending on charge ratio: neg. or pos. (absolute value higher)	Pos. -> pos. (absolute value higher)
1N48S	Core-shell -> sphere	0.064 -> 0.051	Pos. -> depending on charge ratio: neg. or pos. (absolute value higher)	Pos. -> depending on charge ratio: neg. or pos. (absolute value higher)	If structural change: absolute value higher No structural change: absolute value slightly higher
2N36S	Core-shell -> core-shell	0.17 -> 0.10	Pos. -> depending on charge ratio: neg. or pos. (absolute value higher)	Pos. -> neg. (absolute value higher)	No structural change: absolute value slightly higher
2N68S	Core-shell -> core-shell	0.23 -> 13	Pos. -> neg. (absolute value higher)	Neg. -> neg. (absolute value higher)	No structural change: absolute value slightly higher
2N368S	sphere -> sphere	0.22 -> 0.10	Neg. -> neg. (absolute value higher)	Pos. -> depending on charge ratio: neg. or pos. (absolute value higher)	No structural change: absolute value slightly higher

ITC Analysis

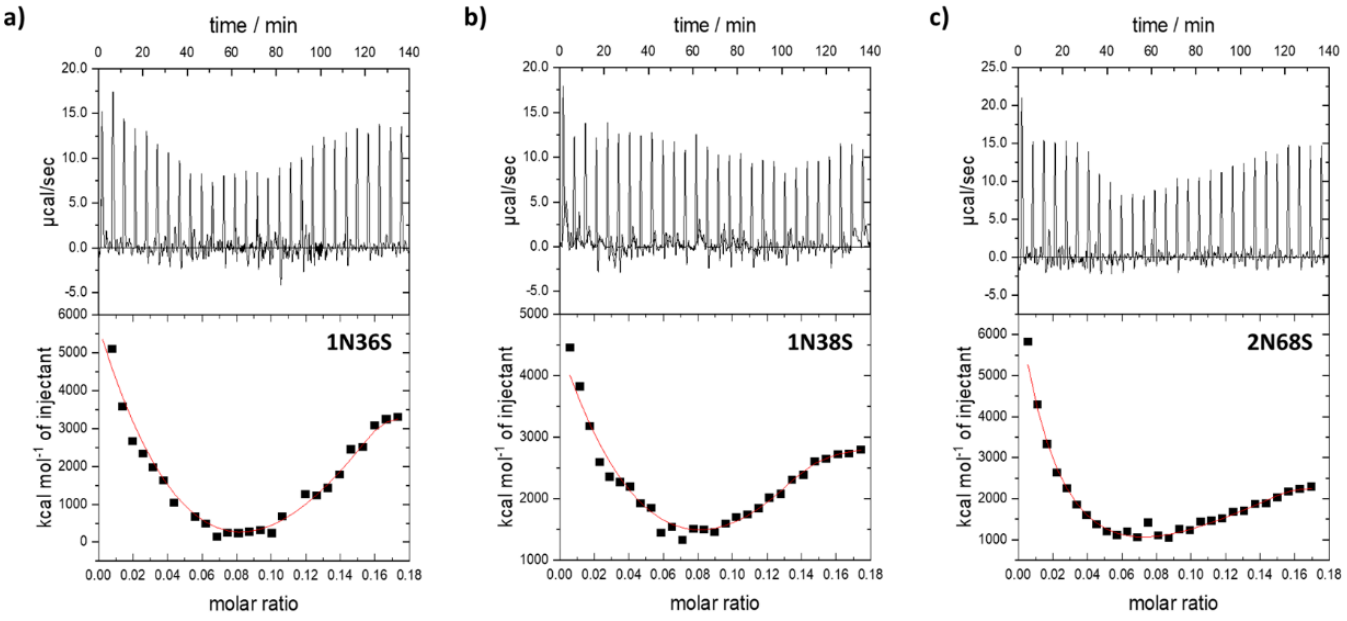

Figure S13: ITC of the photoacid-macroion assembly with a) 1N36S, b) 1N38S, and c) 2N68S before irradiation with the raw data on top and the fitted results below. The concentration of the photoacids was c(photoacids) = $2 \cdot 10^{-5}$ mol/l in the cell, while the concentration of the dendrimer in the syringe is c(dendrimer) = $1 \cdot 10^{-5}$ mol/l. The molar ratio is the ratio between the concentration of the photoacid and the dendrimer.

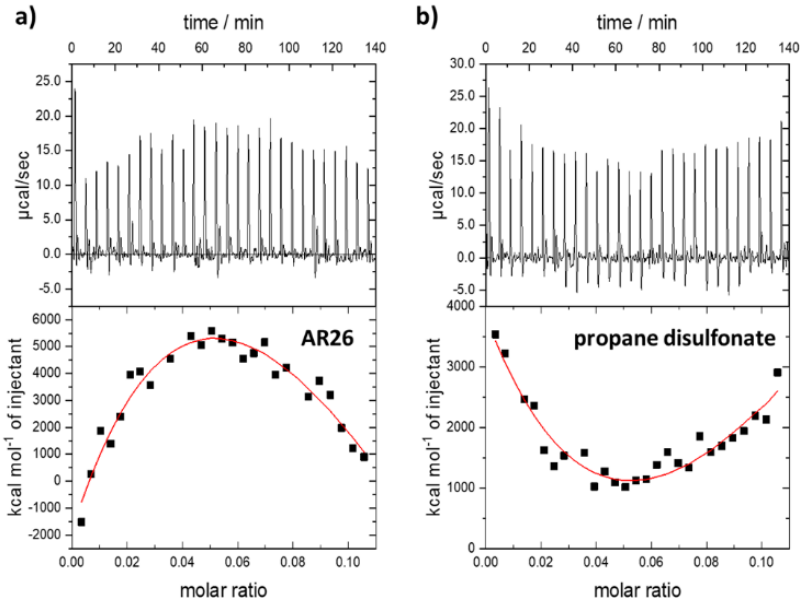

Figure S14: Comparison ITC: ITC of disulfonate-macroion assembly with a) AR26 and b) propane disulfonate before irradiation with the raw data on top and the fitted results below. The concentration of the small molecules were c(molecules) = $2 \cdot 10^{-5}$ mol/l in the cell, while the concentration of the dendrimer in the syringe is c(dendrimer) = $1 \cdot 10^{-5}$ mol/l. The molar ratio is the ratio between the concentration of the photoacid and the dendrimer

Table S4: Thermodynamic analysis of the photoacid-dye association by ITC for the divalent photoacids: Full ITC results

	1N38S	**1N48S**	**1N36S**	**2N36S**	**2N68S**
ΔH_1 / (kJ/mol)	86.3 ± 3.4	86.9 ± 5.7	98.9 ± 8.2	88.9 ± 4.4	80.2 ± 6.4
ΔS_1 / (kJ/mol/K)	0.36 ± 0.02	0.36 ± 0.01	0.40 ± 0.04	0.36 ± 0.03	0.34 ± 0.04
ΔH_2 / (kJ/mol)	-144.1 ± 22	-143.7 ± 14	-152.5 ± 16	-150.0 ± 11	-139.9 ± 23
ΔS_2 / (kJ/mol/K)	-0.42 ± 0.02	-0.41 ± 0.04	-0.45 ± 0.03	-0.43 ± 0.04	-0.40 ± 0.05
ΔH_3 / (kJ/mol)	48.7 ± 2.2	48.1 ± 4.7	45.9 ± 2.1	47.7 ± 1.6	42.5 ± 3.4
ΔS_3 / (kJ/mol/K)	0.18 ± 0.07	0.18 ± 0.03	0.16 ± 0.03	0.16 ± 0.05	0.14 ± 0.05
ΔH_{bind} / (kJ/mol)	-57.8	-56.8	-53.6	-61.1	-59.7
ΔS_{bind} / (kJ/mol/K)	-0.055	-0.052	-0.051	-0.071	-0.069
ΔG_{bind} / (kJ/mol)	-41.6	-41.7	-38.6	-40.3	-39.4
K_{bind} / M^{-1}	$2.0 \cdot 10^{10}$	$3.2 \cdot 10^{10}$	$4.2 \cdot 10^{10}$	$1.3 \cdot 10^{10}$	$1.9 \cdot 10^{10}$

Dipole Moment Consideration

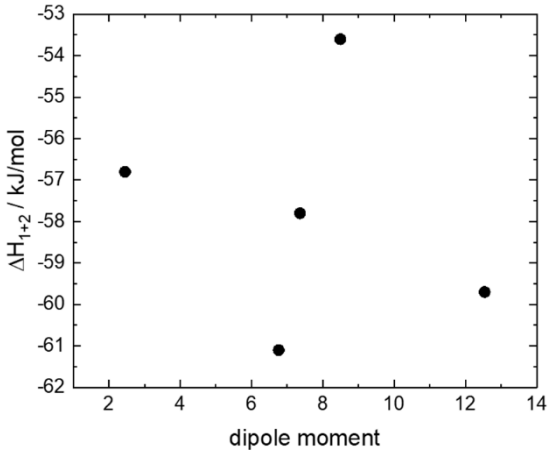

Figure S15: Analysis of secondary interaction of photoacid-macroion assemblies: Dependency of the association enthalpy on the dipole moment (from DFT), showing no clear dependency, i.e. indicating that the dipole moment, does not correlate with the thermodynamics.

PDADMAC-Photoacid Assemblies

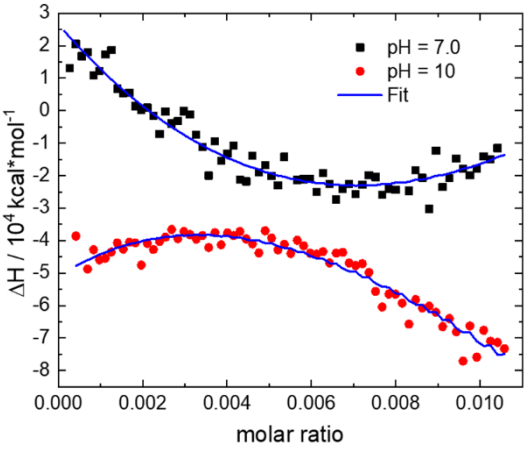

Figure S16: Analysis of PDADMAC-1N36S assemblies: ITC results at pH = 7.0 and pH = 10 before irradiation.

Appendix: Further Dynamic Light Scattering Raw Data

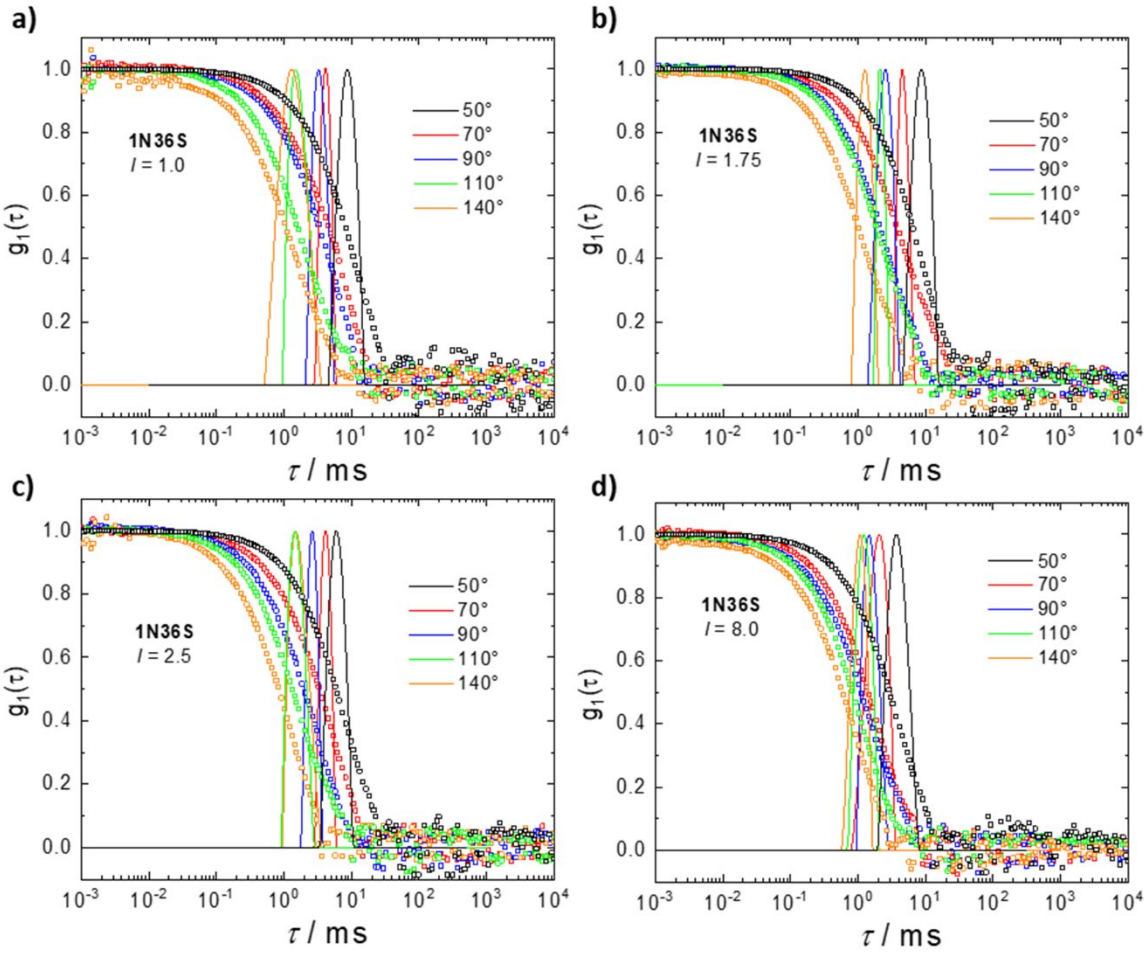

Figure S17: DLS of photoacid-macroion nano-objects for the assemblies with 1N36S at different charge ratios and scattering angles: Charge ratio of a) *I* = 1.0, b) *I* = 1.75, c) *I* = 2.5 and d) *I* = 8.0 before photo-irradiation, electric field autocorrelation function $g_1(\tau)$ and distribution of relaxation times A(τ) at exemplary scattering angles.

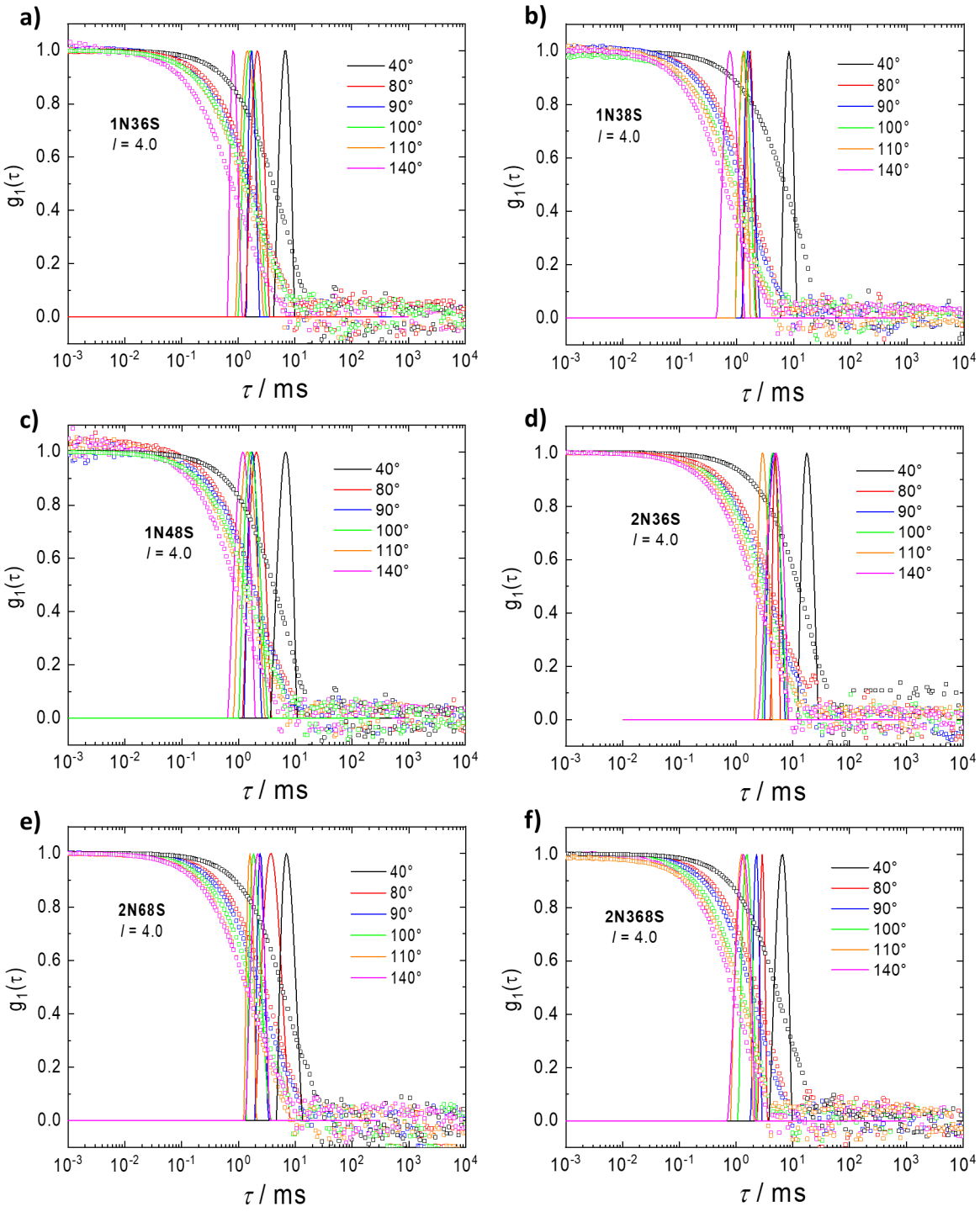

Figure S18: DLS of photoacid-macroion nano-objects of the various photoacids at a charge ratio of *l* = 4.0 before photo-irradiation: Electric field autocorrelation function $g_1(\tau)$ and distribution of relaxation times A(τ) at exemplary scattering angles with a) 1N36S, b) 1N38S, c) 1N48S, d) 2N36S e) 2N68S and f) 2N368S.

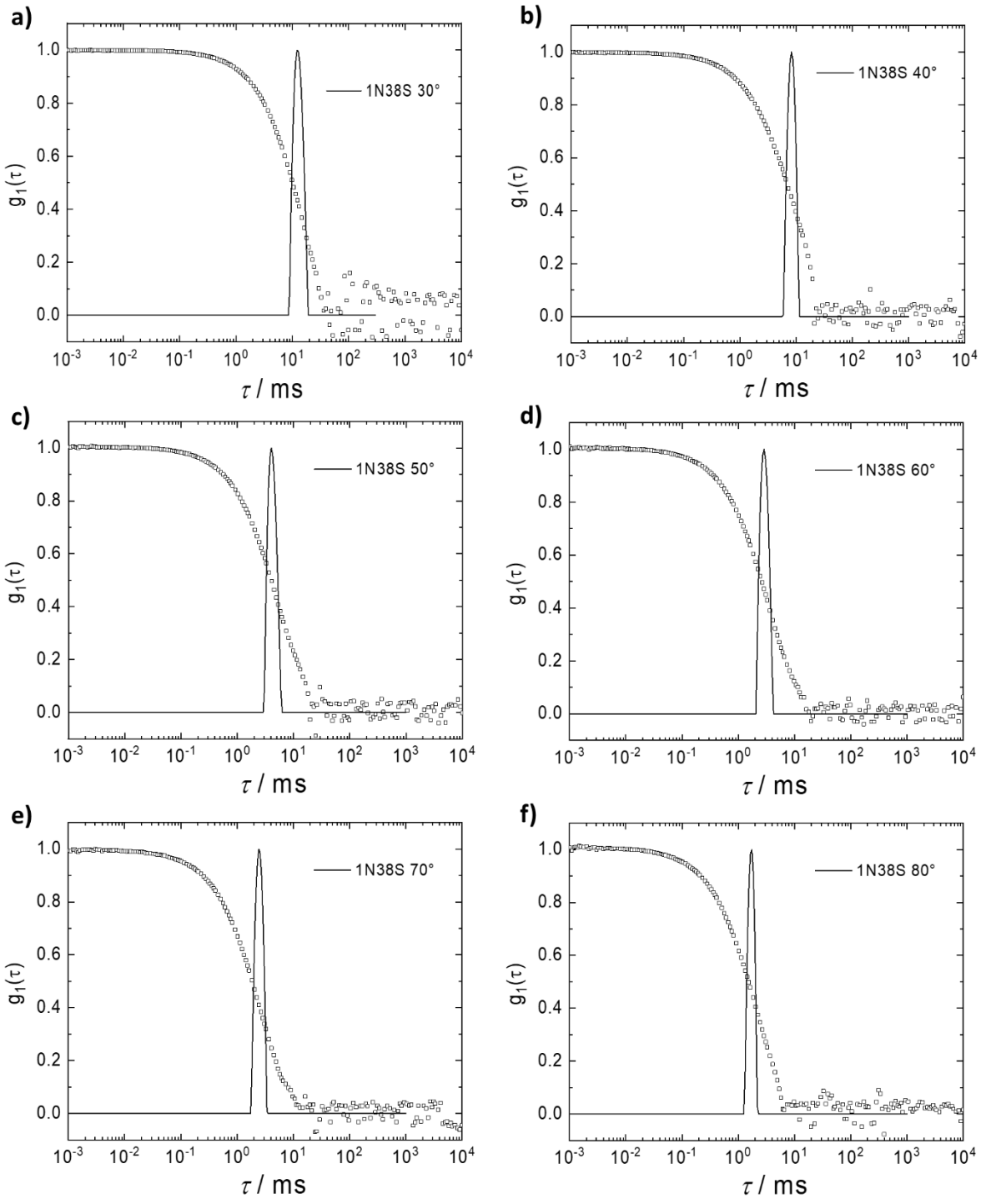
a)
1N38S 30°
b)
1N38S 40°
c)
1N38S 50°
d)
1N38S 60°
e)
1N38S 70°
f)
1N38S 80°
g1(τ)
τ / ms

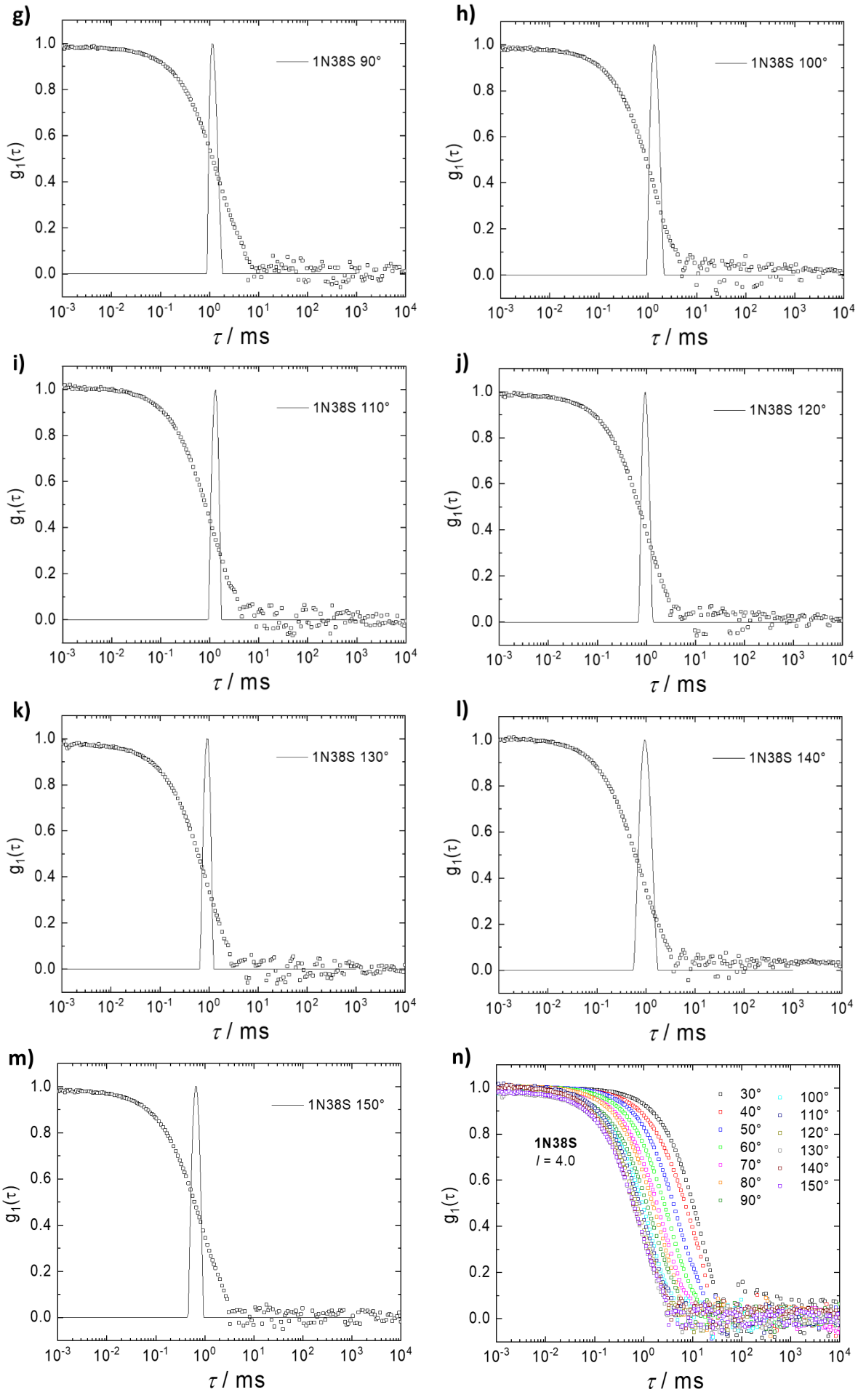
g)
1N38S 90°
h)
1N38S 100°
i)
1N38S 110°
j)
1N38S 120°
k)
1N38S 130°
l)
1N38S 140°
m)
1N38S 150°
n)
1N38S
I = 4.0
30°
40°
50°
60°
70°
80°
90°
100°
110°
120°
130°
140°
150°
g1(τ)
τ / ms

Figure S19: DLS of a photoacid-macroion nano-object sample for all scattering angles: assemblies with 1N38S before photo-irradiation, electric field autocorrelation function $g_1(\tau)$ and distribution of relaxation times $A(\tau)$ for a) 30°, b) 40°, c) 50°, d) 60°, e) 70°, f) 80°, g) 90°, h) 100°, i) 110°, j) 120°, k) 130°, l) 140°, m) 150° and n) all autocorrelation functions for $30° \leq \theta \leq 150°$.

References

[81] C. E. Foster, G. Wright, K. Johnson, M. E. Raggatt, P. Patel, WO2004078859 (A1), **2004**.

[82] W. Burchard, M. Schmidt, W. H. Stockmayer, *Macromolecules* **1980**, *13*, 580.

[83] S. Bantle, M. Schmidt, W. Burchard, *Macromolecules* **1982**, *15*, 1604.

[84] W. Burchard in *Adv. Polym. Sci.*, Springer Berlin Heidelberg, Berlin, Heidelberg, **1983**, pp. 1–124.

[85] K. Huber, W. Burchard, L. J. Fetters, *Macromolecules.* **1984**, *17*, 541.

[86] J. M. Schurr, K. S. Schmitz, *Annu. Rev. Phys. Chem.* **1986**, *37*, 271.

[87] P. N. Pusey, W. van Megen, *Phys. A: Stat. Mech.* **1989**, *157*, 705.

[88] K. S. Schmitz, *Introduction to Dynamic Light Scattering by Macromolecules*, Elsevier, **1990**.

[89] M. Antonietti, S. Heinz, M. Schmidt, C. Rosenauer, *Macromoecules.* **1994**, *27*, 3276.

[90] J. Jansson, K. Schillén, M. Nilsson, O. Söderman, G. Fritz, A. Bergmann, O. Glatter, *J. Phys. Chem. B* **2005**, *109*, 7073.

[91] Z. Li, H. Cheng, J. Li, J. Hao, L. Zhang, B. Hammouda, C. C. Han, *J. Phys. Chem. B* **2011**, *115*, 7887.

[92] K. Fischer, M. Schmidt, *Biomaterials* **2016**, *98*, 79.

[93] Y. Mao, K. Liu, C. Zhan, L. Geng, B. Chu, B. S. Hsiao, *J. Phys. Chem. B* **2017**, *121*, 1340.

[94] S. Förster, M. Schmidt, M. Antonietti, *Polymer* **1990**, *31*, 781.

[95] T. A. P. Seery, M. Yassini, T. E. Hogen-Esch, E. J. Amis, *Macromolecules.* **1992**, *25*, 4784.

[96] M. Antonietti, A. Briel, F. Gröhn, *Macromolecules* **2000**, *33*, 5950.

[97] F. Gröhn, M. Agarwal, R. Schweins, A. Zika, *Light-Triggerable Photoacid Nano-Assemblies*, Institut Laue-Langevin (ILL), **2021**.

[98] O. Arnold, J. C. Bilheux, J. M. Borreguero, A. Buts, S. I. Campbell, L. Chapon, M. Doucet, N. Draper, R. Ferraz Leal, M. A. Gigg, V. E. Lynch, A. Markvardsen, D. J. Mikkelson, R. L. Mikkelson, R. Miller, K. Palmen, P. Parker, G. Passos, T. G. Perring, P. F. Peterson, S. Ren, M. A. Reuter, A. T. Savici, J. W. Taylor, R. J. Taylor, R. Tolchenov, W. Zhou, J. Zikovsky, *Nucl. Instrum. Methods. Phys. Res. A* **2014**, *764*, 156.

[99] F. Akeroyd, S. Ansell, S. Antony, O. Arnold, A. Bekasovs, J. Bilheux, J. Borreguero, K. Brown, A. Buts, S. Campbell, D. Champion, L. Chapon, M. Clarke, S. Cottrell, R. Dalgliesh, D. Dillow, M. Doucet, N. Draper, R. Fowler, M. A. Gigg, G. Granroth, M. Hagen, W. Heller, A. Hillier, S. Howells, S. Jackson, D. Kachere, M. Koennecke, C. Le Bourlot, R. Leal, V. Lynch, P. Manuel, A. Markvardsen, R. McGreevy, D. Mikkelson, R. Mikkelson, R. Miller, S. Nagella, T. Nielsen, K. Palmen, P. G. Parker, M. Pascal, G. Passos, T. Perring, P. F. Peterson, F. Pratt, T. Proffen, P. Radaelli, J. Rainey, S. Ren, M. Reuter, L. Sastry, A. Savici, J. Taylor, R. J. Taylor, M. Thomas, R. Tolchenov, R. Whitley, M. Whitty, S. Williams, W. Zhou, J. Zikovsky, *Mantid: Manipulation and Analysis Toolkit for Instrument Data*, Mantid Project, **2013**.

[100] G. F. André Guinier, *Small-Angle Scattering of X-Rays. Structure of matter series*, John Wiley and Sons, New-York, **1955**.

[101] J. J. Snellenburg, S. P. Laptenok, R. Seger, K. M. Müllen, I. H. M. van Stokkum, *J. Stat. Soft.* **2012**, *49*.

[102] Z. R. Grabowski, W. Rubaszewska, *J. Chem. Soc., Faraday Trans. 1* **1977**, *73*, 11.

[103] Th. Förster, *Zeitschrift für Elektrochemie und angewandte physikalische Chemie* **1950**, *54*, 42.

[104] L. M. Tolbert, J. E. Haubrich, *J. Am. Chem. Soc.* **1994**, *116*, 10593.

[105] S. G. Schulman, L. S. Rosenberg, W. R. Vincent, *J. Am. Chem. Soc.* **1979**, *101*, 139.

[106] R. Knochenmuss, I. Fischer, D. Lührs, Q. Lin, *Isr. J. Chem.* **1999**, *39*, 221.